Inorganic Chemistry

ARTICLE

pubs.acs.org/IC

Structure and Properties of Single Crystalline $CaMg_2Bi_2$, $EuMg_2Bi_2$, and $YbMg_2Bi_2$

Andrew F. May,*[,†] Michael A. McGuire,[†] David J. Singh,[†] Radu Custelcean,[‡] and Gerald E. Jellison, Jr.[†]

[†]Materials Science and Technology Division and [‡]Chemical Sciences Division, Oak Ridge National Laboratory, Oak Ridge, Tennessee 37831, United States

Supporting Information

ABSTRACT: Single crystals of $CaMg_2Bi_2$, $EuMg_2Bi_2$, and $YbMg_2Bi_2$ were obtained from a Mg−Bi flux cooled to 650 °C. These materials crystallize in the $CaAl_2Si_2$ structure-type ($P\bar{3}m1$, No. 164), and crystal structures are reported from refinements of single crystal and powder X-ray diffraction data. $EuMg_2Bi_2$ displays an antiferromagnetic transition near 7 K, which is observed via electrical resistivity, magnetization, and specific heat capacity measurements. Magnetization measurements on $YbMg_2Bi_2$ reveal a weak diamagnetic moment consistent with divalent Yb. Despite charge-balanced empirical formulas, all three compounds are *p*-type conductors with Hall carrier concentrations of $2.0(3) \times 10^{19}$ cm^{-3} for $CaMg_2Bi_2$, $1.7(1) \times 10^{19}$ cm^{-3} for $EuMg_2Bi_2$, and $4.6(7) \times 10^{19}$ cm^{-3} for $YbMg_2Bi_2$, which are independent of temperature to 5 K. The electrical resistivity decreases with decreasing temperature and the resistivity ratios $\rho(300\ \mathrm{K})/\rho(10\ \mathrm{K}) \leq 1.6$ in all cases, indicating significant defect scattering.

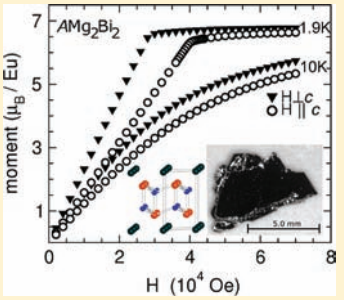

INTRODUCTION

The $CaAl_2Si_2$ structure-type (trigonal, No. 164, $P\bar{3}m1$) has been heavily investigated from the point of view of inorganic chemistry. The "umbrella" bonding about Si is particularly interesting,[1,2] as is the variety of compositions which form in this structure. Antimonides with the $CaAl_2Si_2$ structure-type became of interest to the thermoelectrics community with the publication of modest thermoelectric efficiency in $Ca_xYb_{1-x}Zn_2Sb_2$ near $T = 775$ K,[3] followed by higher efficiency in $EuZn_2Sb_2$.[4] The high temperature transport properties in the AZn_2Sb_2 (A = Sr, Ca, Yb, Eu) materials are discussed in ref 5, and several other studies have reported data for the analogous ACd_2Sb_2 systems and their solid solutions,[6−8] with a zT of 1.2 at 700 K observed in $YbCd_{1.6}Zn_{0.4}Sb_2$.[9] In general, complex materials whose bonding can be understood using the Zintl formalism are of interest to the thermoelectric community,[10−12] particularly since the discovery of high thermoelectric efficiency in the $Yb_{14}MnSb_{11}$ system.[13,14]

The Zintl formalism provides a simple picture for bonding in the $CaAl_2Si_2$-type materials. In the case of $CaMg_2Bi_2$, for instance, a covalent layer of $[Mg_2Bi_2]^{2-}$ is supported by charge transfer from the layer of Ca^{2+}. Calculations in the analogous AZn_2Sb_2 series suggest charge transport is not entirely complete,[5] and that these compounds have a fairly strong covalent character between the "ionic" layers. Detailed discussions of bonding in this family have been provided.[1,2]

Despite significant research on ternary Sb-based Zintl compounds,[15−27] analogous Bi-based materials have received less attention.[28] In this class of materials, the crystal structures of alkaline earth-based AMg_2Bi_2 (A = Mg, Ca, Sr, Ba) have been reported,[29,30] but those of the rare-earth analogues $EuMg_2Bi_2$ and $YbMg_2Bi_2$ have not. Hulliger speculated the existence of these divalent rare-earth derived compounds based on reports of $CaMg_2Bi_2$ and isostructural pnictides containing Yb or Eu.[31] Motivated by the lack of fundamental data in a common family of materials, this study was undertaken to characterize the basic physical and crystallographic properties of the title compounds. First principles calculations are also employed to probe the electronic structure and optical absorption characteristics of $CaMg_2Bi_2$.

Obtaining single crystals large enough for transport measurements is typically a difficult task for novel compositions, particularly when little is known about the (ternary) phase diagrams. The metal-flux method has been utilized to synthesize single crystals of similar ternary compounds, and is particularly useful for exploratory chemistry or difficult to synthesize systems.[32,33] Given the success of an FeAs flux for the growth of large crystals of the $BaFe_2As_2$ superconductors,[34] self-fluxes of excess Mg−Bi were explored. Unlike $BaFe_2As_2$, however, these crystals do not cleave easily and typically grow in three-dimensional forms with one flat face (inset Figure 1), which is identified by X-ray diffraction measurements as the *ab*-plane (see Figure 1). This morphology is consistent with the idea that there is bonding between layers and the materials are more three-dimensional than a crystal structure image (inset Figure 1) or electron counting argument may suggest.

METHODS

Single crystals were obtained via the metal-flux method using nominal melt compositions of AMg_4Bi_6, where A = Ca, Yb, or Eu. The growth occurred in Al_2O_3 crucibles sealed within evacuated silica ampules over a

Received: August 3, 2011
Published: October 14, 2011

dx.doi.org/10.1021/ic2016808 | *Inorg. Chem.* 2011, 50, 11127–11133

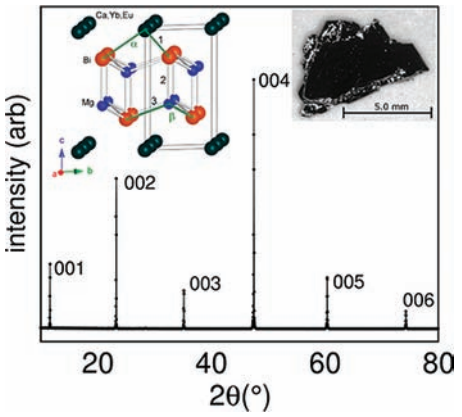

Figure 1. Representative PXRD data from an as-grown facet of $CaMg_2Bi_2$ demonstrating the (00 L) orientation, an image of which is shown in the inset. The inset presents a crystal structure image with the unit cell outlined, and bond distances (1,2,3) and angles (α,β) are labeled for discussion in the text and Table 3.

total of ~43 h. The raw elements were heated to 900 °C, and the ampules were removed from the furnace at 650 °C for centrifugation. Growth is believed to occur below ~750 °C for these compositions because centrifugation at 750 °C did not yield any crystals; the melt was cooled from 750 to 650 °C over 24 h. Additional details are provided in the Supporting Information.

The crystals typically had one flat face (identified as the *ab*-plane, Figure 1), with a range of sizes observed (0.5−8 mm), and the side opposite this face was generally three-dimensional, often with steps visible to the naked eye; intergrown crystals were not uncommon. The Ca- and Eu-based compounds tended to grow larger crystals than did the Yb-based compound. Some smaller crystals grew with two parallel faces, allowing transport measurements on as-grown crystals; for measurements on larger crystals, polishing was necessary and a flat face was used to orient the crystal. The crystals were found to be stable in air for a period of several hours, with $CaMg_2Bi_2$ tarnishing more quickly than the Eu- or Yb-based compounds. However, after prolonged exposure to air, the crystals become brittle, and thus crystals were kept under dynamic vacuum or in a helium glovebox between measurements.

Crystal structures were characterized via single crystal X-ray diffraction at 173 K using a Bruker SMART APEX CCD diffractometer with Mo-$K\alpha$ radiation (λ = 0.71073 Å). Absorption corrections were applied with SADABS, and the data were refined using SHELXL-97.[35] Powder X-ray diffraction (PXRD) data were collected on as-grown facets and hand-ground crystals at ambient conditions on a PANalytical X'Pert Pro MPD using an incident beam Cu $K_{\alpha,1}$ monochromator, and were refined using the program FullProf.[36] Energy dispersive X-ray measurements on a Hitachi TM-3000 tabletop microscope equipped with a Bruker Quantax 70 EDS system revealed compositions within instrument resolution of the empirical formulas AMg_2Bi_2. Thermal stability to 800 °C was briefly examined via differential thermal analysis (DTA) in a Perkin-Elmer Pyris Diamond TG/DTA, run under flowing argon at a heating rate of 40 °C/min. No strong DTA signals were observed, and the crystals' shapes remained intact after the measurement. However, some reaction between the crystals and the Al_2O_3 powder covering them was observed.

Electronic structure calculations were performed relativistically with the all-electron general potential linearized augmented planewave (LAPW) method,[37] using the WIEN2k code,[38] and include spin−orbit coupling for all elements. A standard generalized gradient approximation (GGA) functional is used to relax the internal coordinates in the unit cell by total energy minimization. This was done using the experimental lattice parameters of ref 30 and the GGA of Perdew and co-workers (PBE).[39] The relaxed coordinates were within 1% of those in Supporting Information, Table 5. The resulting structural parameters are used to calculate the electronic structure and optical absorption (optical package of the WIEN2k code) using the recently developed modified Becke Johnson functional of Tran and Blaha, denoted TB-mBJ here.[40] Unlike standard GGA functionals, which are designed to reproduce total energies and structures but underestimate the band gaps of semiconductors,[41] the TB-mBJ functional cannot be used for total energy calculations, but does yield very much improved band gaps in a wide variety of materials.[40,42,43]

Table 1. Selected Data from Refinements of Single Crystal X-ray Diffraction on $CaMg_2Bi_2$, $YbMg_2Bi_2$, and $EuMg_2Bi_2$ at 173 K[a]

empirical formula	$CaMg_2Bi_2$	$EuMg_2Bi_2$	$YbMg_2Bi_2$
a (Å)	4.7236(3)	4.7716(3)	4.7258(4)
c (Å)	7.6512(10)	7.8365(12)	7.6453(14)
vol (Å^3)	147.84(2)	154.52(3)	147.87(3)
density (g/cm^3)	5.69	6.65	7.18
extinction coeff	0.027	0.007	0.024
R_{int}	0.0261	0.0481	0.0378
R_1 (all data)	0.0146	0.0192	0.0172
wR_2 (all data)	0.0327	0.0486	0.0437
goodness of fit	1.209	1.189	1.071
highest peak/deepest hole	1.44/−1.88	2.79/−1.32	1.80/−1.39
data/restraints/params	172/0/10	177/0/10	172/0/10
reflections/uniq. refl.	1352/172	1375/177	1332/172

[a] Lattice parameters in parentheses are from PXRD at 300 K. Space group No. 164, $P\bar{3}m1$.

Electrical transport was probed via Hall coefficient (R_H) and electrical resistivity (ρ) measurements, which were performed from 300 to 5 and 2 K, respectively, in a Quantum Design Physical Property Measurement System (PPMS). Hall coefficients were obtained from a fit of the Hall resistance versus magnetic field, with maximum fields of ±6 T employed. To gain insight into the diversity of transport properties for a given growth, the room temperature electrical resistivity and Hall coefficient (at ±0.5 T) on approximately four as-grown crystals of each composition were measured via the van der Pauw configuration. When all measurement requirements were met, similar values were observed in both the PPMS and the van der Pauw setup at 300 K for a given crystal. High quality contacts (2−10 Ω) were made with DuPont 4929N silver paste. Finally, a Quantum Design Magnetic Properties Measurements System (MPMS) was utilized to examine the magnetic behavior between 300 and 1.9 K.

RESULTS AND DISCUSSION

Crystal and Electronic Structures. The title compounds AMg_2Bi_2 form in the $CaAl_2Si_2$ structure (space group $P\bar{3}m1$, No. 164), which is shown in the inset of Figure 1. As shown in Table 1, little variation is observed in the lattice parameters of the Ca- and Yb-based compounds, while the Eu-based compound has an expanded unit cell, which is consistent with the atomic radii.[44] The structural parameters obtained from refinements of single-crystal X-ray diffraction data are presented in Table 1 and Table 2, while data from PXRD are provided in the Supporting Information, Table 5.

The lattice parameters of $CaMg_2Bi_2$ have been previously reported as a = 4.73 Å and c = 7.68 Å.[30] PXRD data (at ambient conditions) obtained on hand-ground crystals agree with this previous report, with lattice constants and uncertainties obtained

Table 2. Refined Structural Parameters for $CaMg_2Bi_2$, $YbMg_2Bi_2$, and $EuMg_2Bi_2$ from Single-Crystal X-ray Diffraction Data at T = 173 K

		atomic coordinates			$U_{11} = U_{22} = 2U_{12}$	U_{33}	U_{eq}
	atom	x	y	z	Å^2	Å^2	Å^2
$CaMg_2Bi_2$	Ca	0	0	0	0.0129(8)	0.008(1)	0.0112(5)
	Mg	1/3	2/3	0.6301(5)	0.013(1)	0.008(2)	0.0114(7)
	Bi	1/3	2/3	0.24130(4)	0.0091(2)	0.0065(3)	0.0083(2)
$EuMg_2Bi_2$	Eu	0	0	0	0.0101(3)	0.0082(4)	0.0095(3)
	Mg	1/3	2/3	0.6276(5)	0.013(1)	0.008(2)	0.0110(8)
	Bi	1/3	2/3	0.24992(4)	0.0082(3)	0.0068(3)	0.0077(2)
$YbMg_2Bi_2$	Yb	0	0	0	0.0088(3)	0.0116(4)	0.0097(2)
	Mg	1/3	2/3	0.6308(5)	0.007(1)	0.014(2)	0.0092(8)
	Bi	1/3	2/3	0.24119(5)	0.0058(3)	0.0095(3)	0.0070(2)

Table 3. Bond Distances and Angles from Single-Crystal X-ray Diffraction Data at T = 173 K[a]

	bond distance (Å)		bond angle (deg)	
$CaMg_2Bi_2$	Ca−Bi (1)	3.2933(3)	Bi−Ca−Bi (α)	91.64(1)
	Mg−Bi (2)	2.975(4)	Bi−Mg−Bi (β)	109.09(7)
	Mg−Bi (3)	2.899(1)		
$EuMg_2Bi_2$	Eu−Bi (1)	3.3801(3)	Bi−Eu−Bi (α)	89.79(1)
	Mg−Bi (2)	2.960(4)	Bi−Mg−Bi (β)	109.73(7)
	Mg−Bi (3)	2.917(1)		
$YbMg_2Bi_2$	Yb−Bi (1)	3.2931(3)	Bi−Yb−Bi (α)	91.70(1)
	Mg−Bi (2)	2.979(4)	Bi−Mg−Bi (β)	109.20(7)
	Mg−Bi (3)	2.899(1)		
Mg_3Bi_2	Mg−Bi (1)	3.207	Bi−Mg−Bi (α)	93.36
	Mg−Bi (2)	2.923	Bi−Mg−Bi (β)	108.572
	Mg−Bi (3)	2.874		

[a] Literature data for Mg_3Bi_2 are included,[29] and bond distances and angles are labeled in Figure 1.

from Rietveld refinements of a = 4.7308(1) Å and c = 7.6720(2) Å obtained for $CaMg_2Bi_2$ at 300 K, while single crystal diffraction on this compound at 173 K resulted in a = 4.7236(3) Å and c = 7.6512(10) Å. A small Bi peak was observed in the ground crystals, likely from the surfaces which were sometimes visibly contaminated with residue from the flux. Rietveld refinements of powder diffraction data on $EuMg_2Bi_2$ yielded a = 4.7771(1) Å and c = 7.8524(1) Å, and for $YbMg_2Bi_2$ refinement yielded a = 4.7321(1) Å and c = 7.6606(1) Å. For comparison, in $EuMg_2Sb_2$ a = 4.695(1) Å and c = 7.724(1) Å,[27] and thus it is clear that Bi expands the lattice relative to Sb.

The bond distances and angles in these AMg_2Bi_2 compounds can be relatively easily understood in terms of atomic radii. The bonds and bond angles are summarized in Table 3 and labeled in the crystal structure in Figure 1. It is observed that the Bi−A bond (bond 1) is largest in the Eu-based material. The metallic radii of Eu is ∼2.084 Å compared to the ∼1.970 Å and 1.933 Å for Ca and Yb. For comparison, data for Mg_3Bi_2 are included,[29] and the A−Bi bond decreases as expected; Mg is expected to have a radius of 1.598 Å.[44] The Mg−Bi bond distances within the covalent layer (bonds 2,3) vary little as the A site is changed, and are longer in the c direction (bond 2) then in the basal plane (bond 3). This indicates a distortion of the tetrahedral coordination around Mg.

To quantify the structural distortions, we consider the octahedral and tetrahedral coordination of Bi around A and Mg, respectively. Both bond angles and ratio of ligand or bond distances can be used to examine the distortion of these features. For the octahedral environment, Mg_3Bi_2 displays the largest deviation from the ideal octahedral angle of 90° (here, this is α in Figure 1), and the ratio of Bi−Bi ligand distances is also furthest from the ideal value of unity (not shown). The size of Eu^{2+} is nearly ideal for this octahedral coordination, with ligand Bi−Bi distances differing by less than 0.4%, and the bond angles approaching the ideal 90°.

The larger Eu^{2+} ion expands the structure in the ab-plane, increasing the distance between Bi atoms. Maintaining optimal Mg−Bi distances then results in the observed flattening of the $(Mg_2Bi_2)^{2-}$ layer. This behavior is observed in the basal plane Bi−Mg−Bi angle (angle β), which is less than the ideal 109.5° for A = Mg, Ca, or Yb, while for A = Eu it is greater than the ideal angle. As the large Eu^{2+} flattens the Mg−Bi layer, the result is a shorter Mg−Bi bond along the c-axis (bond 2), and a larger basal plane angle (Bi−Mg−Bi, β) in the tetrahedron. Despite significant deviation from the ideal tetrahedral angle in Mg_3Bi_2, the ratio of Mg−Bi bond distances is nearly as close to unity as it is for A = Eu, which highlights the flexibility of the Mg bonding. Indeed, the formation of Mg_3Bi_2 reveals the ability of Mg to display chemistry similar to that of both d^{10} transition metals (Zn,Cd) and electropositive alkaline/rare earth metals (Ca,Yb).

The LAPW band structure for $CaMg_2Bi_2$ is shown in Figure 2a, and the associated density of states ($N(E)$) is shown in Figure 2b. $CaMg_2Bi_2$ displays a direct band gap of 0.7 eV, which originates primarily from charge transfer, though there is some covalency between the Mg and Bi states. As observed in the density of states, bismuth states dominate the valence band edge, and some Bi character is observed in the conduction band indicating Mg and Bi covalency. Figure 2b includes the interstitial contribution, which accounts for the $N(E)$ that does not fall within any LAPW sphere. This contribution arises primarily from extended Mg/Ca p and s states. The $N(E)$ peak at ∼3 eV is due to Ca d states. LAPW sphere radii of 2.5 bohr for Ca and Mg, and 2.8 bohr for Bi were utilized.

The optical absorption spectrum obtained from the electronic structure, including only the allowed electric dipole transitions, is shown in Figure 2c. The onset of strong absorption occurs at energies significantly higher than the fundamental gap. However, the conduction band minimum is formed by a rather dispersive (light) band, with another dispersive band just above it, and

dx.doi.org/10.1021/ic2016808 |Inorg. Chem. 2011, 50, 11127–11133

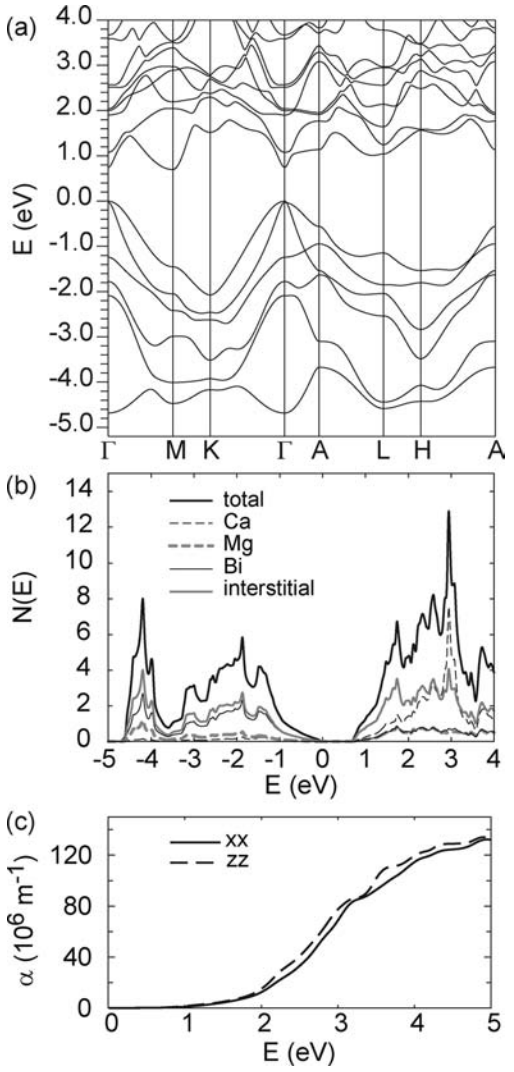

Figure 2. (a) Calculated band structure for $CaMg_2Bi_2$ as obtained using the TB-mBJ functional, and (b) the density of states $N(E)$, including projections onto the LAPW spheres and the interstitial contribution. (c) The resulting absorption spectrum shows strong absorption occurring away from the conduction band edge where heavy conduction bands contribute. The Fermi energy is located at 0 eV.

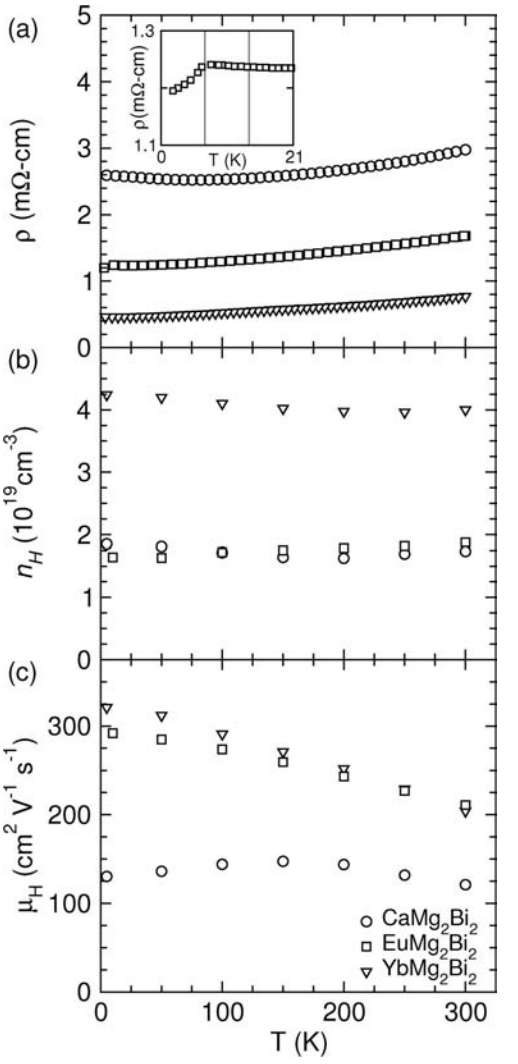

Figure 3. Electrical properties of $CaMg_2Bi_2$, $EuMg_2Bi_2$, and $YbMg_2Bi_2$ from 1.9 to 300 K. Representative curves are shown for (a) electrical resistivity, (b) Hall carrier concentration, and (c) Hall mobility. Relatively large residual resistivities can be inferred from the plots, indicating a large defect concentration, which is consistent with the fairly high Hall carrier concentration for nominally charged-balanced systems.

heavier bands further above the conduction band edge (note the heavier bands at Γ at ~2 eV in Figure 2a). As a result, even though the direct band gaps are ~0.7 eV, the absorption is weak up to almost 2 eV.

Electrical Resistivity and Hall Coefficient. The electrical transport properties of the title compounds are shown in Figure 3 for measurements in the *ab*-plane of single crystals. These compounds are *p*-type conductors with Hall carrier concentrations of approximately 2×10^{19} cm^{-3} in $CaMg_2Bi_2$ and $EuMg_2Bi_2$, and roughly double that in $YbMg_2Bi_2$, as shown in Table 4. They can be considered heavily-doped semiconductors or "poor metals", as the electrical resistivity decreases with decreasing temperature while the carrier concentration remains constant. While the Zintl formalism predicts these materials to be semiconductors, a small defect concentration is likely responsible for the free carriers. This picture is consistent with the lack of carrier freeze-out at low temperatures (the Hall coefficient was measured to 5 K for A = Ca, Yb and 10 K for A = Eu). Indeed, even in $CaMg_2Bi_2$, where a slight increase in the electrical resistivity is observed at low T, the Hall carrier concentration does not change. This upturn in ρ at low T was reproduced, and its origin is unknown.

A distribution of values for the electrical properties for each compound is reported in Table 4. These data are the result of van der Pauw and four-point measurements at room temperature on multiple crystals from the same growth (measurements in the *ab*-plane). While some spread exists, the trend for larger μ_H in the rare-earth based compounds is clear, as is the trend for higher n_H in $YbMg_2Bi_2$. The source for larger mobility in systems with 4f electrons remains unclear, and similar trends have been observed in polycrystalline AZn_2Sb_2.[5] It is unlikely, however, that the f states dominate the valence band edge, which is composed primarily of Bi p-character in $CaMg_2Bi_2$ (see Figure 2b). It is worth noting, though, that in $YbZn_2Sb_2$ the Yb 4f states extend to the gap and make a non-negligible contribution to the valence band edge.[45] In general, one would expect the 4f states to promote heavy electronic bands and thus lower mobility, as well

dx.doi.org/10.1021/ic2016808 |*Inorg. Chem.* 2011, 50, 11127–11133

Table 4. Summary of Data Obtained from Measurements on Single Crystals[a]

compound	n_H 10^{19} cm^{-3}	μ_H $cm^2\ V^{-1}\ s^{-1}$	ρ mΩ cm	ρ(300 K)/ρ (10 K)	Θ_D K
$CaMg_2Bi_2$	1.7−2.3	90−120	2.8−3.3	1.2	244
$EuMg_2Bi_2$	1.6−1.8	180−210	1.7−2.2	1.4	211
$YbMg_2Bi_2$	3.9−5.2	150−200	0.8−0.9	1.6	207

[a] Electrical data are from room temperature measurements, and the Debye temperatures are obtained by fitting C_P between 20 and 200 K.

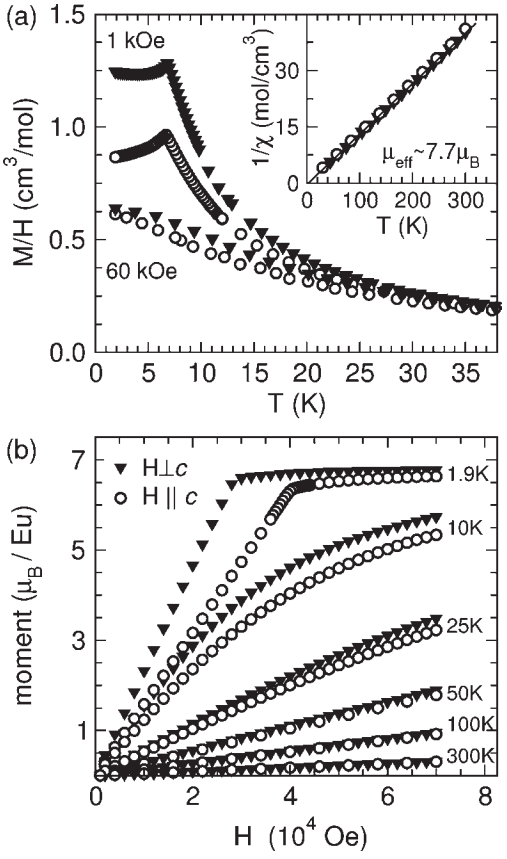

Figure 4. (a) Temperature dependence of **M**/**H** showing the antiferromagnetic transition at ∼7 K and anisotropy at low T and **H** in $EuMg_2Bi_2$. (b) The field dependence of the magnetic moment per Eu reveals a saturation near the expected 7.0 μ_B/Eu. A larger field is required to saturate the moment when **H** || c, and the corresponding decrease in **M**/**H** is observed in panel (a). Regardless of direction, an effective moment of ∼7.7 μ_B/Eu is obtained from the modified Curie−Weiss law (inset, for 1 kOe).

as increased carrier scattering from the spin-disorder associated with Eu^{2+}. The change in resistivity associated with the magnetic transition in $EuMg_2Bi_2$ can be seen in the inset of Figure 3a. It seems most likely that the lower mobility in the $CaMg_2Bi_2$ compound is the result of increased defect scattering. Indeed, while the increase in μ_H with decreasing T is due to the scattering of holes by phonons, the values of μ_H are strongly influenced by a temperature-independent, residual resistance (from defect scattering) that strongly reduces the mobility. This concept is readily observed via the resistivity ratios, which reveal the extent to which the defect scattering influences the mobility at room temperature. The resistivity ratio is low in all compounds (ρ(300 K)/ρ(10 K) ≤ 1.6), but is particularly low for $CaMg_2Bi_2$; these values are summarized in Table 4. The residual resistances are clearly important for thermoelectric application, where reduced mobility directly reduces thermoelectric efficiency.

The types of defects producing the charge carriers have not been identified. It seems probable that *A* or Mg vacancies are responsible for the free carriers. Refinement of the single crystal diffraction data did not warrant inclusion of reduced occupancy for one site as opposed to another. Even for the highest carrier concentration observed (*A* = Yb), only 1 vacancy per 300 atoms would explain the carrier concentration and thus diffraction data are unlikely to provide the evidence required to speculate further. Given that the species occupying the *A*-site affects the carrier mobility, it seems more likely that vacancies of the *A* species are responsible for the carriers, and not Mg vacancies. It is possible different defects are present in each material, though it is also possible that the different compounds respond differently to vacancies on the same site. As discussed below, the Debye temperature is observed to be larger in $CaMg_2Bi_2$ than it is in $EuMg_2Bi_2$ and $YbMg_2Bi_2$, and it is possible this elastic property would be important in understanding the local environment surrounding defects. In terms of electron−phonon scattering, a higher Debye temperature or sound velocity is classically associated with larger carrier mobility,[46] though in this case the defect scattering significantly influences the overall mobility and likely masks these effects at modest temperatures.

Magnetic Properties. Results of magnetization measurements on $EuMg_2Bi_2$ single crystals are shown in Figure 4. Behavior similar to that shown here has been reported for oriented crystals of the isostructural compound $EuZn_2Sb_2$ embedded in a ZnSb matrix.[47] Figure 4a shows the temperature dependence of the magnetic susceptibility (**M**/**H**) below 35 K with the field oriented parallel and perpendicular to the crystallographic *c*-axis. At higher temperatures, isotropic paramagnetic behavior is observed (Figure 4a, inset). At lower temperatures, anisotropic behavior is observed, especially at lower applied fields (Figure 4a,b).

For low-fields the temperature dependence shows a cusp in **M**/**H** that indicates an antiferromagnetic (AFM) transition at T_N ∼7 K; in $EuMg_2Sb_2$ an AFM transition is observed near 8.2 K.[27] The continued decrease in **M**/**H** along the *c*-direction and near temperature independence of **M**/**H** in the *ab*-plane upon cooling below T_N suggest the ordered magnetic moments are aligned along the *c*-axis.

At higher applied fields the measured moment saturates (Figure 4b) and the antiferromagnetic transition is no longer observed (Figure 4a). The linear field dependence of the measured moment at 1.9 K and below the saturation field indicates a field-induced, continuous reorientation of the ordered moments. A similar field-dependence was reported for $EuFe_2As_2$ at low temperatures, in which saturation of the moment is achieved near 1.7 T for **H**|| c and slightly less for **H**⊥c.[48,49] The magnetic anisotropy noted above results in a different field required to saturate the moments parallel and perpendicular to the *c*-axis, but the saturation value of ∼6.7 μ_B per Eu is independent of orientation. This is close to the value of 7.0 μ_B expected for divalent Eu.

At temperatures well above T_N, the magnetic susceptibility is independent of orientation and is well described by a Curie−Weiss law with a temperature independent offset (**M**/**H** = χ_0 + (C)/(T − θ)). Fitting the data collected in an applied field of 1

dx.doi.org/10.1021/ic2016808 |*Inorg. Chem.* 2011, 50, 11127–11133

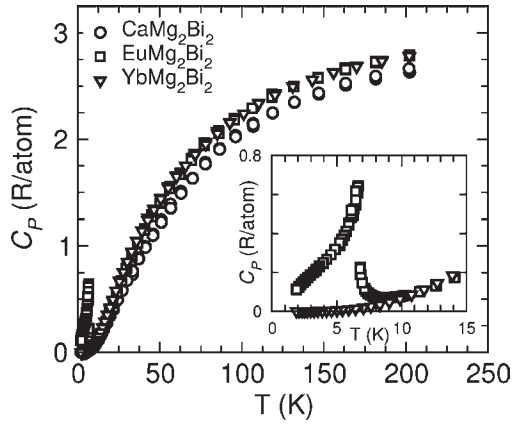

Figure 5. Heat capacity of $CaMg_2Bi_2$ is slightly suppressed relative to that of $YbMg_2Bi_2$ and $EuMg_2Bi_2$, though all approach the value of 3R/atom at high temperatures. The inset emphasizes the antiferromagnetic transition in $EuMg_2Bi_2$ near 6.7 K, which provides a large peak in C_P because of the large $J = {}^7/_2$ for Eu^{2+}.

kOe over a temperature range of 50−300 K gives an effective moment of 7.7(1) μ_B per Eu, close to the expected value of 7.94 μ_B for Eu^{2+}. The temperature independent offset χ_0 is negative and is on the order of 10^{-4} cm^3/mol. The fitted Weiss temperature (θ) is near zero, consistent with the low ordering temperature of $T_N \sim 7$ K.

Magnetization measurements on $YbMg_2Bi_2$ showed temperature independent diamagnetism over most of the temperature range investigated, indicating nonmagnetic, divalent Yb. The magnitude of the susceptibility (10^{-4} cm^3/mol) is consistent with estimates based on core diamagnetism. A weak paramagnetic component is observed at low temperatures, likely from small amounts of magnetic impurities or the presence of some trivalent Yb. Assuming all of the magnetism is due to trivalent Yb, an upper bound on the concentration of Yb^{3+} of ~2% is obtained.

Heat Capacity. The specific heat capacity C_P of the title compounds are shown in Figure 5, where the expected behavior is observed in all compounds and C_P approaches the simple theoretical limit of 3R/atom at high temperature. A slight suppression in C_P is observed in $CaMg_2Bi_2$ relative to the rare-earth compounds, which was confirmed with additional measurements. The smaller C_P in $CaMg_2Bi_2$ can be treated as an increase in the Debye temperature (Θ_D). The Debye model for specific heat, which fails to quantitatively describe the complete temperature dependence of C_P, is particularly informative for elucidating the trends in a given material system. The Debye model for a solid with N_{at} atoms per formula unit and reduced phonon energy x is

$$C = 9RN_{at}\left(\frac{T}{\Theta_D}\right)^3 \int^{\Theta_D/T} \frac{x^4 e^x}{(e^x - 1)^2}\,dx \qquad (1)$$

The Debye temperature of $CaMg_2Bi_2$ is larger than that of $EuMg_2Bi_2$ and $YbMg_2Bi_2$ when C_P data above ~20 K are considered. In Table 4, values of Θ_D obtained by fitting C_P between 20 and 200 K are provided; this temperature range was selected to avoid complications associated with the magnetic transition in $EuMg_2Bi_2$. For comparison, the low-temperature limit obtained by fitting a line to C_P/T versus T^2 between roughly 1.9 and 4 K yields values of 189 and 191 K for $CaMg_2Bi_2$ and $YbMg_2Bi_2$, respectively. At low temperatures, eq 1 becomes $C = 12\pi^4 RN_{at}T^3/(5\Theta_D{}^3)$ and thus the slope of C_P/T versus T^2 provides the low-temperature limit of the Debye temperature. The intercept of C_P/T versus T^2 is the Sommerfeld coefficient γ which is related to the electronic contribution to the specific heat. The low-temperature fits for A = Ca and Yb resulted in $\gamma \approx 0$, which is consistent with the modest carrier concentrations observed.

The antiferromagnetic transition in $EuMg_2Bi_2$ is observed as a large peak in the heat capacity C_P near 6.7 K, as shown in the inset of Figure 5. The lack of transition in $YbMg_2Bi_2$ further confirms the existence of nonmagnetic Yb^{2+}, and allows the $YbMg_2Bi_2$ data to be used as a baseline for the analysis of the phase transition in $EuMg_2Bi_2$. Specifically, the entropy change ΔS for the transition from the low S antiferromagnetic state to a paramagnetic state is estimated as $\Delta S = \int_{1.9}^{12}(C_{P,Eu122} - C_{P,Yb122})/T\,dT = 14.3$ J/mol/K. This value is consistent with basic theory, which estimates S for a simple paramagnet as $S = R\ln[2J + 1]$;[50] $J = {}^7/_2$ for Eu^{2+} and thus the simple description provides $\Delta S \approx S_{para} = 17.3$ J/mol/K.

SUMMARY

Single crystals of $CaMg_2Bi_2$, $EuMg_2Bi_2$, and $YbMg_2Bi_2$ were grown in a Mg−Bi flux, and their properties were characterized. The changes in bond distance and angle can be understood in terms of atomic radii, and the Eu-based materials have the least distorted octahedra surrounding the A-sites. An antiferromagnetic transition in $EuMg_2Bi_2$ is clearly observed near 7 K, and the entropy change estimated from the heat capacity is consistent with simple paramagnetic theory. Electronic structure calculations predict $CaMg_2Bi_2$ to be a direct-gap semiconductor with a band gap of ~0.7 eV. However, the nominally charged-balanced crystals were observed via electrical property measurements to be heavily defected, with Hall carrier concentrations in the range of 2 to 5 × 10^{19} cm^{-3} and resistivity ratios $\rho(300\text{ K})/\rho(10\text{ K}) \leq 1.6$, with the lowest value observed for $CaMg_2Bi_2$; $CaMg_2Bi_2$ also possesses the highest Debye temperature. The electrical properties of these materials are similar to the $A(Zn,Cd)_2Sb_2$ compounds which display moderate thermoelectric efficiency, and thus the thermoelectric behavior of these materials warrants investigation.

ASSOCIATED CONTENT

Supporting Information. Crystallographic data in CIF format. Further details are given about the synthesis, the powder diffraction refinement results, and the electronic structure calculations. This material is available free of charge via the Internet at http://pubs.acs.org.

AUTHOR INFORMATION

Corresponding Author
*E-mail: mayaf@ornl.gov.

ACKNOWLEDGMENT

We thank Brian Sales for useful discussions. This research was sponsored by the Laboratory Directed Research and Development Program of Oak Ridge National Laboratory, managed by UT-Battelle, LLC, for the U.S. Department of Energy (A.F.M., M.A.M., G.E.J.). D.J.S. was supported by the U.S. Department of

Energy, Office of Basic Energy Sciences, Materials Sciences and Engineering Division. R.C. was supported by the Division of Chemical Sciences, Geosciences, and Biosciences, Office of Basic Energy Sciences, U.S. Department of Energy.

REFERENCES

(1) Zheng, C.; Hoffmann, R.; Nesper, R.; von Schnering, H.-G. *J. Am. Chem. Soc.* **1986**, *108*, 1876–1884.
(2) Burdett, J. K.; Miller, G. J. *Chem. Mater.* **1990**, *2*, 12–26.
(3) Gascoin, F.; Ottensmann, S.; Stark, D.; Haile, S. M.; Snyder, G. J. *Adv. Funct. Mater.* **2005**, *15*, 1860–1864.
(4) Zhang, H.; Zhao, J.-T.; Grin, Y.; Wang, X.-J.; Tang, M.-B.; Man, Z.-Y.; Chen, H.-H.; Yang, X.-X. *J. Chem. Phys.* **2008**, *129*, 164713.
(5) Toberer, E. S.; May, A. F.; Melot, B.; Flage-Larsen, E.; Snyder, G. J. *Dalton Trans.* **2010**, *39*, 1046–1054.
(6) Zelinska, O. Y.; Tkachuk, A. V.; Grosvenor, A. P.; Mar, A. *Chem. Mer. Alloys* **2008**, *1*, 204–209.
(7) Zhang, H.; Fang, L.; Tang, M.-B.; Chen, H.-H.; Yang, X.-X.; Guo, X.; Zhao, J.-T.; Grin, Y. *Intermetallics* **2010**, *18*, 193–198.
(8) Cao, Q.-G.; Zhang, H.; Tang, M.-B.; Chen, H.-H.; Yang, X.-X.; Grin, Y.; Zhao, J.-T. *J. Appl. Phys.* **2010**, *107*, 053714.
(9) Wang, X.-J.; Tang, M.-B.; Chen, H.-H.; Yang, X.-X.; Zhao, J.-T.; Burkhardt, U.; Grin, Y. *Appl. Phys. Lett.* **2009**, *94*, 092106.
(10) Toberer, E. S.; May, A. F.; Snyder, G. J. *Chem. Mater.* **2010**, *22*, 624–634.
(11) Toberer, E. S.; Snyder, G. J. *Nat. Mater.* **2008**, *7*, 105–114.
(12) Kleinke, H. *Chem. Mater.* **2010**, *22*, 604–211.
(13) Brown, S. R.; Kauzlarich, S. M.; Gascoin, F.; Snyder, G. J. *Chem. Mater.* **2006**, *18*, 1873–1877.
(14) Toberer, E. S.; Cox, C. A.; Brown, S. R.; Ikeda, T.; May, A. F.; Kauzlarich, S. M.; Snyder, G. J. *Adv. Funct. Mater.* **2008**, *18*, 2795–2800.
(15) Lam, R.; Mar, A. *Inorg. Chem.* **1996**, *35*, 6959–6963.
(16) Yi, T.; Cox, C. A.; Toberer, E. S.; Snyder, G. J.; Kauzlarich, S. M. *Chem. Mater.* **2010**, *22*, 935–941.
(17) Kim, S.-J.; Hu, S.; Uher, C.; Kanatzidis, M. G. *Chem. Mater.* **1999**, *11*, 3154–3159.
(18) Wang, X.-J.; Tang, M.-B.; Zhao, J.-T.; Chen, H.-H.; Yang, X.-X. *Appl. Phys. Lett.* **2007**, *90*, 232107.
(19) Saparov, B.; Bobev, S.; Ozbay, A.; Nowak, E. R. *J. Solid State Chem.* **2008**, *181*, 2690–2696.
(20) Toberer, E. S.; May, A. F.; Scanlon, C.; Snyder, G. J. *J. Appl. Phys.* **2009**, *105*, 063701.
(21) May, A. F.; Toberer, E. S.; Snyder, G. J. *J. Appl. Phys.* **2009**, *106*, 013706.
(22) Toberer, E. S.; May, A. F.; Melot, B.; Flage-Larsen, E.; Snyder, G. J. *Dalton Trans.* **2010**, *39*, 1046–1054.
(23) Saparov, B.; Xia, S.-Q.; Bobev, S. *Inorg. Chem.* **2008**, *47*, 11237–11244.
(24) Zevalkink, A.; Toberer, E. S.; Zeier, W. G.; Flage-Larsen, E.; Snyder, G. J. *Energy Environ. Sci.* **2011**, *4*, 510–518.
(25) Ganguli, A. K.; Gupta, S.; Corbett, J. D. *Inorg. Chem.* **2006**, *45*, 196–200.
(26) Kim, S.-J.; Kanatzidis, M. G. *Inorg. Chem.* **2001**, *40*, 3781–3785.
(27) Wartenberg, F.; Kranenberg, C.; Pocha, R.; Johrendt, D.; Mewis, A.; Hoffmann, R.-D.; Mosel, B. D.; Pöttgen, R. *Z. Naturforsch.* **2002**, *57b*, 1270–1276.
(28) Zelinska, O. Y.; Mar, A. *Inorg. Chem.* **2008**, *47*, 297–305.
(29) Zintl, E.; Husemann, E. *Z. Phys. Chem., Abt. B* **1933**, *21*, 138–155.
(30) Deller, K.; Eisenmann, B. *Z. Naturforsch., B* **1977**, *32b*, 612–616.
(31) Hulliger, F. *Handbook on the Physics and Chemistry of Rare Earths*; North Holland Publishing Company: Amsterdam, The Netherlands, 1979; Vol. 4; Chapter 33.
(32) Canfield, P. C.; Fisher, I. R. *J. Cryst. Growth* **2001**, *225*, 155–161.
(33) Kanatzidis, M. G.; Pöttgen, R.; Jeitschko, W. *Angew. Chem., Int. Ed.* **2005**, *44*, 6996–7023.
(34) Sefat, A. S.; Jin, R.; McGuire, M. A.; Sales, B. C.; Singh, D. J.; Mandrus, D. *Phys. Rev. Lett.* **2008**, *101*, 117004.
(35) Sheldrick, G. M. *Acta Crystallogr.* **2008**, *A64*, 112–122.
(36) Rodríguez-Carvajal, J. *Phys. B* **1993**, *192*, 55–69.
(37) Singh, D. J.; Nordstrom, L. *Planewaves, Pseudopotentials and the LAPW Method*, 2nd ed.; Springer Verlag: Berlin, Germany, 2006.
(38) Blaha, P.; Schwarz, K.; Madsen, G.; Kvasnicka, D.; Luitz, J. *WIEN2k, An Augmented Plane Wave + Local Orbitals Program for Calculating Crystal Properties*; Vienna University of Technology: Vienna, Austria, 2001.
(39) Perdew, J. P.; Burke, K.; Ernzerhof, M. *Phys. Rev. Lett.* **1996**, *77*, 3865.
(40) Tran, F.; Blaha, P. *Phys. Rev. Lett.* **2009**, *102*, 226401.
(41) Perdew, J. P.; Chevary, J. A.; Vosko, S. H.; Jackson, K. A.; Pederson, M. R.; Singh, D. J.; Fiolhais, C. *Phys. Rev. B* **1992**, *46*, 6671.
(42) Singh, D. J. *Phys. Rev. B* **2010**, *82*, 155145.
(43) Singh, D. J. *Phys. Rev. B* **2010**, *82*, 205102.
(44) Pauling, L. *J. Am. Chem. Soc.* **1947**, *69*, 542–553.
(45) Flage-Larsen, E.; Diplas, S.; Prytz, O.; Toberer, E. S.; May, A. F. *Phys. Rev. B* **2010**, *81*, 205204.
(46) Fistul, V. I. *Heavily Doped Semiconductors*; Plenum Press: New York, 1969.
(47) Weber, F.; Cosceev, A.; Drobnik, S.; Faißt, A.; Grube, K.; Nateprov, A.; Pfleiderer, C.; Uhlarz, M.; Löhneysen, H. v. *Phys. Rev. B* **2006**, *73*, 014427.
(48) Ren, Z.; Zhu, Z.; Jiang, S.; Xu, X.; Tao, Q.; Wang, C.; Feng, C.; Cao, G.; Xu, Z. *Phys. Rev. B* **2008**, *78*, 052501.
(49) Jiang, S.; Luo, Y.; Ren, Z.; Zhu, Z.; Wang, C.; Xu, X.; Tao, Q.; Cao, G.; Xu, Z. *New J. Phys.* **2009**, *11*, 025007.
(50) Smart, J. S. *Effective Field Theories of Magnetism*; W. B. Saunders Company: New York, 1966.
(51) Singh, D. *Phys. Rev. B* **1991**, *43*, 6388.